Nanoscale

COMMUNICATION

View Article Online
View Journal | View Issue

Cite this: *Nanoscale*, 2023, **15**, 14338

Received 14th June 2023,
Accepted 5th August 2023

DOI: 10.1039/d3nr02840b

rsc.li/nanoscale

Scalable engineering of hierarchical layered micro-sized silicon/graphene hybrids *via* direct foaming for lithium storage†

Mathar Hamza,‡[a,b] Siyuan Zhang,‡[a,b] Wenqiang Xu,[a] Denghui Wang,[a,b] Yingjie Ma *[a] and Xianglong Li *[a,b]

Low-cost micro-sized silicon is an attractive replacement for commercial graphite anodes in advanced lithium-ion batteries (LIBs) but suffers from particle fracture during cycling. Hybridizing micro-sized silicon with conductive carbon materials, especially graphene, is a practical approach to overcome the volume change issue. However, micro-sized silicon/graphene anodes prepared *via* the conventional technique encounter sluggish Li^+ transport due to the lack of efficient electrolyte diffusion channels. Here, we present a facile and scalable method to establish efficient Li^+ transport channels through direct foaming from the laminated graphene oxide/micro-sized silicon membrane followed by annealing. The conductive graphene layers and the Li^+ transport channels endow the composite material with excellent electronic and ionic conductivity. Moreover, the interconnected graphene layers provide a robust framework for micro-sized silicon particles, allowing them to transform decently in the graphene layer space. Consequently, the prepared hybrid material, namely foamed graphene/micro-sized Si (f-G-Si), can work as a binder-free and free-standing anode without additives and deliver remarkable electrochemical performance. Compared with the control samples, micro-sized silicon wrapped by laminated graphene layers (G-Si) and commercial micro-sized Si, f-G-Si maximizes the utilization of silicon and demonstrates superior performance, disclosing the role of Li^+ diffusion channels. This study sheds light on the rational design and manufacture of silicon anodes and beyond.

Introduction

Lithium-ion batteries (LIBs) have attracted significant attention towards supplying the power requirement of electric vehicles, consumer electronics, and utility-scale storage.[1–3] The performance of LIBs mainly relays on their electrode materials, especially anode materials. Currently, graphite dominates the anode material market, but its limited capacity (~370 mA h g^{-1}) cannot satisfy the increasing demand for high-performance LIBs.[4] Alternative anode materials, such as silicon (Si), pure metals, and chalcogenides, have been investigated to overcome current capacity limitations. Among these emerging anode materials, Si has been regarded as the most promising alternative to graphite-based anodes because of its large reversible capacity (4200 mA h g^{-1}), satisfactory working potential, and low cost.[5–7] Despite its attractive characteristics, Si is still impeded in practical applications due to its poor intrinsic ionic and electrical conductivity that restricts Li-ion and electron diffusion kinetics and the dramatic volume change (400%) during the repeated lithiation/de-lithiation processes, which results in fracture, pulverization, and eventually capacity fading.[8,9] It is a challenge to simultaneously achieve enhanced capacity, good rate capability, and excellent stability with Si-based anode materials.[10]

Consequently, Si-based composite materials employing conductive carbon materials as supports or coating layers have been developed to improve the sluggish electrode kinetics and buffer the volume changes during the electrochemical reactions.[11–17] These conductive carbon materials, such as graphene, amorphous carbon, and carbon nanotubes, possess outstanding electron and ion conductivity and mechanical properties, thereby excessively boosting the performance of Si anodes.[18–20] Compared with other carbon materials, graphene is a more promising candidate for the fabrication of Si/carbon composite anode materials because of its high conductivity, large surface area, atomic thickness, high mechanical strength, and superb electrochemical stability. Based on its intrinsic characteristics, significantly improved performance

[a]*CAS Key Laboratory of Nanosystem and Hierarchical Fabrication, CAS Center for Excellence in Nanoscience, National Center for Nanoscience and Technology, Beijing 100190, P.R. China. E-mail: lixl@nanoctr.cn, mayj@nanoctr.cn*
[b]*University of Chinese Academy of Sciences, Beijing 100039, P.R. China*

†Electronic supplementary information (ESI) available. See DOI: https://doi.org/10.1039/d3nr02840b

‡These authors contributed equally to this work.

has been achieved with Si/graphene composites.[18–22] Furthermore, Si/graphene anodes can be fabricated without binders, conductive additives, or external weighty metal current collectors, demonstrating advantages in terms of weight, energy density and cost over conventional anodes.[23,24] In addition, the Si/graphene anodes can be fabricated using graphene oxide (GO) as the raw material *via* a low-cost and scalable production process, highly amenable to large-scale applications.[25]

Nevertheless, previous research studies on Si/graphene anodes typically focus on nanostructured Si, such as Si nanoparticles, Si nanowires, and Si nanosheets, because nanostructures can endure the considerable mechanical stress derived from the volume variation due to high surface-to-volume ratio, reducing the crack propagation and subsequently improving the structural stability of Si.[26–28] However, nanostructured Si suffers from low tapping density, high electrical resistance caused by significant interparticle resistance and surface/interface scattering, and low coulombic efficiency (CE) due to its large surface area that induces irreversibility of the initial capacity.[29–31] In contrast, micro-sized Si exhibits a much higher tap density, a smaller surface area and a lower cost, which make it more attractive in industrial applications.[32,33] Nonetheless, micro-sized Si/graphene anodes fabricated *via* conventional methodologies incur sluggish lithium-ion transport due to the lack of efficient channels for electrolyte diffusion, thus providing only limited improvements in performance.[34]

Here, we propose a facile and scalable strategy for the fabrication of hierarchically layered graphene/micro-sized silicon hybrids with efficient electrolyte diffusion channels and a robust structure (Fig. 1a). These durable channels are established *via* direct foaming from the laminated graphene oxide/micro-sized silicon membrane (GO-Si) followed by annealing, producing micro-sized silicon particles encapsulated by delaminated graphene layers, namely a foamed graphene/micro-sized silicon membrane (f-G-Si). The foaming and annealing processes simultaneously generate cross-linked graphene layers (Fig. 1a) and consequently endow f-G-Si with a robust mechanical structure and electron conductive network, enabling f-G-Si to work as a binder-free and free-standing anode without additional conductive agents. Most importantly, the established Li^+ transport channels in f-G-Si endow the micro-sized Si particles with superb ionic conductivity. Furthermore, the robust structure of f-G-Si mitigates the pulverization of micro-silicon particles, significantly overcoming the volume change issues. Thanks to these features, the f-G-Si anode can maximize the utilization of micro-sized Si and deliver an outstanding reversible charge capacity of 2836 mA h g^{-1} at 1 A g^{-1}, a high-rate capability (1522 mA h g^{-1} at 10 A g^{-1}) and remarkable cycling performance. Additionally, low-cost micro-sized Si and GO are chosen as raw materials, and the production process of f-G-Si is facile and scalable. Therefore, our methodology is convenient for large-scale applications.

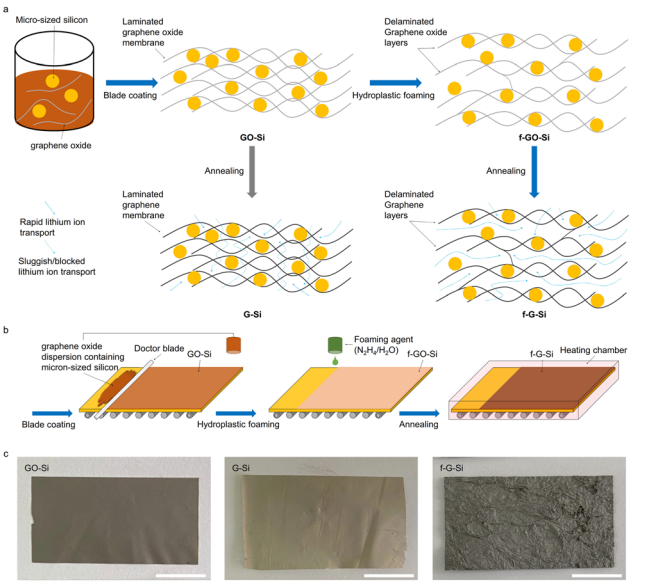

Fig. 1 Strategies for hierarchical layered micro-sized silicon/graphene hybrids. (a) Synthesis and structures of f-G-Si and G-Si and corresponding characteristics for lithium storage. (b) The scalable fabrication process of f-G-Si. (c) Digital photographs of GO-Si, G-Si, and f-G-Si (scale bar: 1 cm).

Results and discussion

As indicated in Fig. 1a, f-G-Si was prepared by directly forming GO-Si and annealing. GO-Si was obtained from the aqueous slurry of commercial micro-sized Si (Fig. S1†) and GO on a polyethylene terephthalate (PET) substrate by the low-cost blade coating method. Subsequently, GO-Si was foamed by immersing in an aqueous hydrazine solution, which generated bubbles because of the reaction of N_2H_4 between oxygen-containing groups of GO sheets. In the subsequent drying process, driven by the capillary force originating from water evaporation, the bubbles were clustered, creating electrolyte diffusion channels named "Li^+ transport channels". Moreover, the capillary force also drove the GO walls of bubbles to bind together, forming a cross-linked hyperboloid structure and thus endowing the composite with a robust structure.[35] Finally, GO in f-GO-Si was reduced into graphene by annealing at 850 °C, yielding the electrically conductive f-G-Si. Notably, the approach is scalable and suitable for large-scale preparation (Fig. 1b), possibly extending to other graphene-based composites. Moreover, f-G-Si and G-Si are mechanically strong and flexible. Thus they are promising robust binder-free and free-standing anodes for LIBs (Fig. 1c). Besides, the thickness of f-G-Si is five-fold that of G-Si (50 μm *vs.* 10 μm) due to the foaming process.

The hierarchical structure of f-G-Si is observed from the scanning electron microscopy (SEM) images (Fig. 2a and Fig. S2†). There is an abundance of interspaces between neighboring graphene layers of f-G-Si, which can act as channels for electrolyte diffusion, benefiting Li^+ transport (Fig. 2a). All the

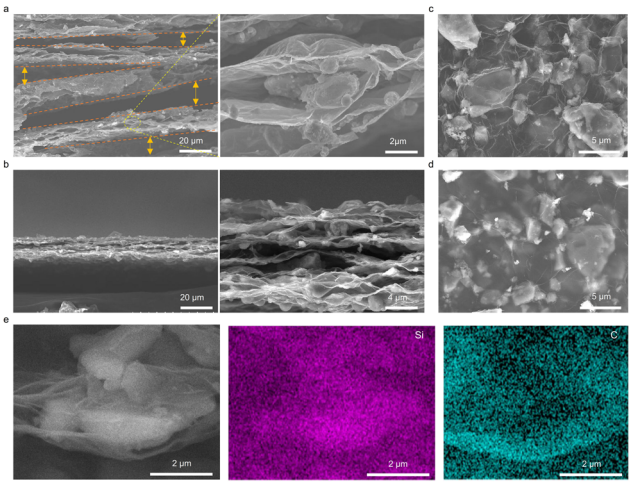

Fig. 2 Cross-sectional SEM images of (a) f-G-Si (the spaces between the neighboring dashed lines are the channels; the enlarged region shows the encapsulated micro-sized silicon particle.) and (b) G-Si; SEM images of the surfaces of (c) f-G-Si and (d) G-Si. SEM images and corresponding EDX mapping of (e) micro-sized silicon particles in f-G-Si.

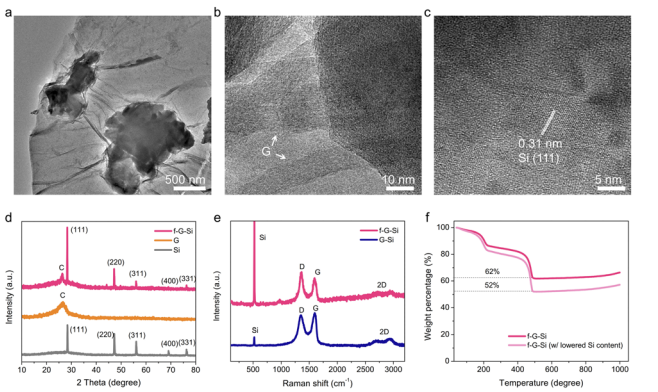

Fig. 3 (a–c) TEM images of f-G-Si, (d) XRD patterns of f-G-Si, G, and Si, (e) Raman spectra of f-G-Si and G-Si, and (f) TGA curves of f-G-Si and G-Si.

micro-silicon particles (Fig. 2a, the enlarged region), even the ones on the top of f-G-Si (Fig. 2c), are encapsulated in delaminated graphene layers with plenty of cells, which can release the volume expansion of Si. A uniform distribution of Si and C elements in the encapsulated Si particle is discovered by scanning electron microscopy-energy dispersive X-Ray spectroscopy (SEM-EDX, Fig. 2e), demonstrating that the graphene sheets interact well with the silicon particle and thus ensuring good electrical contact between them. In contrast, the control sample (G-Si) without the foaming process has a closed-packed structure in which graphene layers are tightly packed together, and the silicon particles are embedded between these packed graphene layers, obviously showing that there is almost no space for electrolyte diffusion (Fig. 2b and d). Brunauer–Emmett–Teller (BET) experiments were carried out under a N_2 atmosphere to identify the structural differences between f-G-Si and G-Si, showing that f-G-Si exhibited a larger specific surface area (3.76 m^2 g^{-1} VS 1.37 m^2 g^{-1}) and larger pores (Table S1a and b†). The above analysis reveals that Li^+ transport channels have been successfully built in f-G-Si *via* the foaming process.

The transmission electron microscopy (TEM) image of f-G-Si shows that each micro-sized Si particle is wrapped by ultra-thin graphene sheets that will minimize the possibility of irreversibly trapping Li^+ (Fig. 3a). Furthermore, the ultra-thin graphene sheets covered Si particles in f-G-Si is thinner than that of G-Si (Fig. S3†), which should arise from the self-structural adjustment of GO layers through plastic slippage during foaming[35]—this process decreases the thickness of graphene sheets that covered micro-sized silicon particles. The high-resolution TEM (HRTEM) image of f-G-Si indicates a well-defined and interconnected network by intercalating Si particles between the graphene layers (Fig. 3b), providing an integrated conductive network for f-G-Si. The HRTEM image of f-G-Si identifies the highly crystalline Si particle, indicating that the crystalline nature of micro-sized Si particles remains after annealing (Fig. 3c). The XRD pattern of f-G-Si also discloses the crystalline structure of Si particles in f-G-Si as the diffraction peaks of f-G-Si matched well with the silicon crystal planes (111), (220), (400), (331), and (311) (Fig. 3d). Raman spectroscopy analysis reveals the graphitic nature of graphene layers in f-G-Si. The ID/IG ratio of f-G-Si is a little higher than that of G-Si (1.07 *vs.* 0.90), suggesting that there are a few more defects in graphene layers of f-G-Si (Fig. 3e). The composition of graphene layers in f-G-Si and G-Si was examined by X-ray photoelectron spectroscopy (XPS). The C1s spectra of f-G-Si and G-Si reveal that the graphene layers in f-G-Si and G-Si display almost the same elemental content (Fig. 4b and d), although there is a little difference in the ID/IG ratio. In addition, *via* XPS analysis, it is found that hydrazine can partially reduce GO in GO-Si during the foaming process as the intensity of the C–O peak decreases after foaming (Fig. S4a and c†). Nevertheless, the partial reduction of GO *via* hydrazine during the foaming process does not affect the elemental content of the final product because of almost the same elemental content of f-G-Si and G-Si. The amount of graphene in f-G-Si is estimated as 38 wt% by thermo-gravimetric analysis (TGA), implying that the Si content in f-G-Si is 62 wt% (Fig. 3f) – the high Si content ensures the increased capacity of f-G-Si. The silicon phases in f-G-Si and G-Si were examined *via* Si 2p XPS analysis (Fig. S5†). The silicon on the surface of G-Si and f-G-Si were oxidized, which were SiO_2 (Fig. S5c†) and SiO_2/Si-Ox (Fig. S5d†), respectively. It should be noted that during foaming, some silicon on the surface of GO-Si was oxidized to Si-Ox (Fig. S5a and b†). Thus, there were three types of silicon (Si, SiO_2, and Si-Ox) in f-GO-Si, all of which were converted into SiO_2 after annealing (Fig. S5b and d†). While silicon on the surface of GO-Si was partially converted to Si-Ox, and thus G-Si contained two types of silicon (SiO_2 and Si-Ox), implying that the foaming process should contribute to the oxidation of silicon on the surface. According to the above analysis, f-G-Si

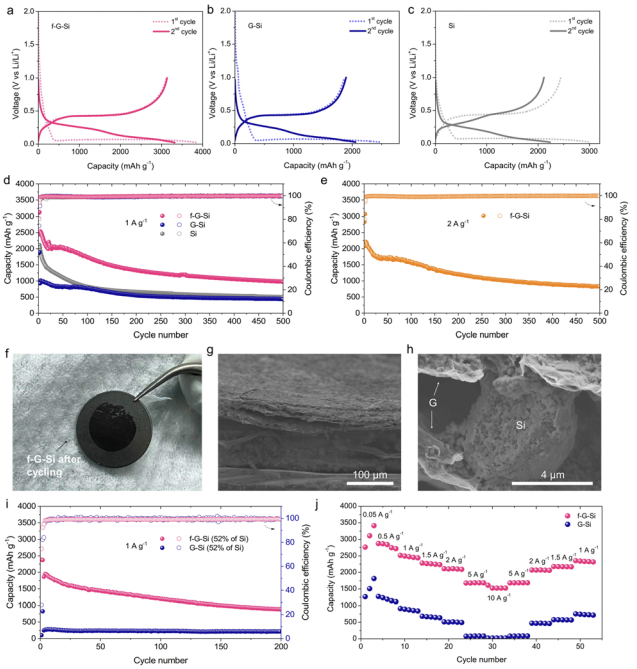

Fig. 4 Electrochemical characterization of anodes. Galvanostatic charge–discharge (GCD) curves of (a) f-G-Si, (b) G-Si, and (c) Si. (d) Cycling performance of f-G-Si, G-Si, and Si anodes at 1 A g^{-1}. (e) Cycling performance of f-G-Si at 2 A g^{-1}. (f) Photo image and (g and h) cross-sectional SEM images of f-G-Si after 200 charge/discharge cycles at 1 A g^{-1}. (i) Cycling performance of f-G-Si and G-Si with a low silicon content (52%) at 1 A g^{-1}. (j) Rate capabilities of f-G-Si and G-Si at current densities ranging from 0.5 to 10 A g^{-1}.

and G-Si exhibit almost the same material composition, and therefore their electrochemical performance is determined by their structural features.

The beneficial effects of the foaming process on f-G-Si were verified by electrochemical tests with two-electrode CR2032 coin-type half-cells in the potential window from 0.01 to 2.0 V (Fig. 4). It should be noted that f-G-Si and G-Si were used as binder-free and free-standing anodes without conductive additives. A conventional silicon anode fabricated with commercial micro-sized Si was chosen as the control sample. As shown in Fig. 4a and b, f-G-Si exhibits a charge capacity of 3114 mA h g^{-1} at a current density of 1 A g^{-1}, much higher than that of the commercial micro-sized Si (2440 mA h g^{-1} at 1 A g^{-1}). The superior capacity is proposed to come from the hierarchical structure of f-G-Si. In f-G-Si, all the commercial micro-sized Si particles are encapsulated by the delaminated graphene layers (Fig. 2a and 3a). The mechanically strong and flexible graphene layers protect the surface of Si particles against electrolyte interactions during charge/discharge processes and mitigate the repeated growth of a solid electrolyte interface (SEI) that leads to Li^+ consumption, consequently giving rise to higher capacity. Among the three anode materials, G-Si displays the lowest capacity (1865 mA h g^{-1} at 1 A g^{-1}), although graphene layers also protect the Si particles inside G-Si. These Si particles are encapsulated by the laminated graphene layers (Fig. 1a and 2b), which should restrict the diffusion of electrolytes to Si particles. They, therefore, make some protected Si particles not accessible to Li^+, leading to limited capacity. The higher capacity of f-G-Si compared to that of G-Si reveals the role of the advanced structure of f-G-Si and the efficient Li^+ transport channels generated *via* foaming. In addition, the free-standing nature of f-G-Si and G-Si makes it unnecessary to use electrochemically active current collectors, binders, and conductive additives and accordingly simplifies the electrode fabrication procedures as well as conduces to their capacity. It can be concluded that the hierarchical structure of f-G-Si can maximize the utilization of Si and achieve much higher capacity than G-Si and commercial micro-sized Si.

As expected, the protection of micro-sized Si particles with graphene layers enables inspiring cycling stability (Fig. 4d and e). f-G-Si still delivers a reversible capacity of 1334 mA h g^{-1} after 200 cycles at 1 A g^{-1}, much higher than that of the commercial micro-sized Si that shows severe degradation during cycling owing to the continuous formation of the SEI layer (660 mA h g^{-1}, Fig. 4d). G-Si also demonstrates good stability during cycling because of the encapsulation with graphene layers, but releases much lower capacity compared with f-G-Si during cycling due to the lack of Li^+ transport channels. At large current densities (Fig. 4e), f-G-Si also presents high cycling stability, providing a capacity of 1200 mA h g^{-1} after 200 cycles at 2 Ag^{-1}. An extended cycling test of up to 500 cycles at different current densities exhibited similar phenomena, highlighting the importance of graphene layers and Li^+ transport channels (Fig. 4e). The delaminated graphene layers of f-G-Si serve as the SEI shielding and volume change buffering shell. The mechanically strong and flexible graphene layers endow f-G-Si with a robust structure that is hard to deform and can maintain stability during long-term cycling (Fig. 4f and g). Besides, the delaminated graphene layers preserve an appropriate void volume compatible with micro-sized Si particles during cycling, confining all the broken Si pieces inside (Fig. 4h) and protecting Si particles from coming in contact with the electrolyte. It should be noted that f-G-Si retained its morphology and thickness even after long-term cycling for up to 500 cycles at 1 Ag^{-1} (Fig. S6a and b†). In contrast, G-Si tripled in thickness after 500 cycles at 1 Ag^{-1} (Fig. S6c and d†), pointing out the role of structural features of f-G-Si in unleashing the potential of micro-sized silicon. Moreover, as mentioned above, the Li^+ transport channels enable the electrolyte to access more Si particles wrapped by ultra-thin graphene layers, generating higher capacity than G-Si during the charge/discharge process. Most importantly, such a high-rate, high-capacity stability level is superior to previous reports on silicon/carbon hybrid anodes (Table S2†).[36–48]

It should be noted that the Li^+ transport channels of f-G-Si are established *via* the foaming process but not by encapsulating micro-sized Si particles with graphene, nevertheless, they can produce some space between the graphene layers (Fig. 2b) because micro-sized silicon particles can act as spacers to separate the graphene sheets. We further tested the electro-

chemical performance of f-G-Si and G-Si containing less micro-sized Si (52 wt%) to confirm this scenario (Fig. 4i and Fig. S7†). If the Li^+ transport channels come from the encapsulation of micro-sized Si particles with graphene, the numbers of the channels should be decreased when fewer micro-sized Si particles are used, thus leading to nominal growth of performance. Without foaming, G-Si containing 52 wt% of micro-sized Si only displays a reversible capacity of 246 mA h g^{-1} at 1 A g^{-1}. In contrast, f-G-Si containing 52 wt% of micro-sized Si presents a much higher capacity of 1951 mA h g^{-1} at 1 A g^{-1}, more than seven fold that of G-Si with 52 wt% of micro-sized Si. f-G-Si containing 52 wt% of micro-sized Si still exhibits a capacity of 885 mA h g^{-1} after 200 cycles at 1 A g^{-1}. The significant enhancement of electrochemical performance when fewer micro-sized Si particles are used implies that the foaming process endues f-G-Si with remarkable capacity but not the encapsulation of micro-sized Si particles with graphene. Without foaming, micro-sized Si particles are tightly encapsulated by laminated graphene layers. As a result, the electrolyte cannot approach some graphene-encapsulated Si particles, decreasing the total capacity.

Establishing Li^+ transport channels is expected to enhance the ionic permeability of f-G-Si. Encapsulating micro-sized Si particles endows f-G-Si with excellent electronic conductivity (Fig. S8†) and allows Si particles and the resulting fractured particles in f-G-Si to remain electrochemically active. Thus, f-G-Si can achieve remarkable capacity and superior rate performance. As shown in Fig. 4j, f-G-Si manifests outstanding rate capability at current densities ranging from 0.5 to 10 A g^{-1}, delivering the discharge-specific capacity of 2872, 2513, 2280, 2111, 1676, and 1522 mA h g^{-1} at 0.5, 1, 1.5, 2, 5 and 10 A g^{-1}, respectively (Fig. S9a†). Moreover, almost a full recovery of the reversible capacity (2513 *vs.* 2353 mA h g^{-1}) can be achieved when the current density is reverted to 1 A g^{-1} from 10 A g^{-1}, firmly corroborating the high reversibility and cycling stability of f-G-Si. By comparison, G-Si exhibits poorer discharge-specific capacity at current densities ranging from 0.5 to 10 A g^{-1}, particularly at large current densities (Fig. S9b†). At 10 A g^{-1}, G-Si becomes electrochemically inactive, implying that the ionic permeability of G-Si is poor. Because both f-G-Si and G-Si own electronically conductive graphene frameworks and there are no apparent differences between the electronic conductivity of f-G-Si and G-Si, revealed by the sheet resistance measured using a four-probe tester (Fig. S8†), the difference in their rate capabilities should originate from their different ionic permeability. We measured the static contact angles between f-G-Si (or G-Si) and the electrolyte to estimate their ionic permeability (Fig. 5a and b). The static contact angle between f-G-Si and an electrolyte droplet is 10°, much lower than that of G-Si (20°), indicating that f-G-Si possesses higher affinity to the electrolyte than G-Si. Additionally, a shorter diffusion time is observed for f-G-Si compared with G-Si (0.5 s *vs.* 1.2 s), which suggests that the electrolyte diffusion in f-G-Si is much more efficient than in G-Si. As a result, the superior rate capability of f-G-Si is derived from its much more efficient Li^+ transport.

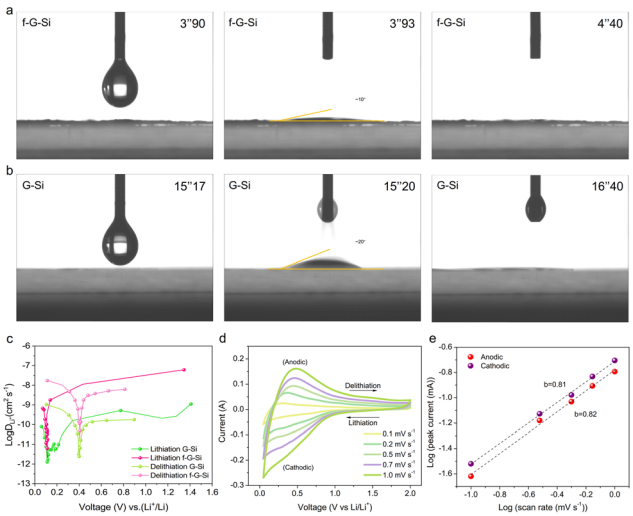

Fig. 5 Electrolyte contact angle and diffusion on (a) f-G-Si and (b) G-Si. (c) Li^+ diffusion coefficients during discharging (lithiation) and charging (delithiation) of f-G-Si and G-Si. (d) CV curves of f-G-Si at different scan rates. (e) Log(*i*) *vs.* log(*v*) curves of cathodic and anodic peaks in d.

The superior rate performance of f-G-Si was confirmed by evaluating the diffusion coefficients of Li^+ in f-G-Si and G-Si *via* the galvanostatic intermittent titration technique (GITT) with a pulse current of 100 mA g^{-1} for 20 min between 20 min rest intervals (Fig. 5c and Fig. S10†). The Li^+ diffusion coefficient of f-G-Si is an order of magnitude higher than that of G-Si, implying much more efficient transport of Li^+ in f-G-Si. This result was also confirmed by electrochemical impedance spectroscopy (EIS) analysis (Fig. S11†). The Nyquist plot obtained from EIS shows that f-G-Si has a smaller charge-transfer resistance than G-Si because of the smaller diameter of the semicircle in the high-frequency region. The kinetic behavior of f-G-Si was investigated *via* a CV test at a scan rate of 0.1 to 1.0 mV s^{-1} in the voltage range of 0.3–1.5 V (Fig. 5d). Similar oxidation/reduction peaks in CV curves of f-G-Si at various scan rates can be observed, showing that f-G-Si exhibits good Li^+ diffusion kinetics. The lithiation/delithiation behavior of f-G-Si was studied by calculating the *b*-value according to the formula ($i = av^b$), which reflected that the electrochemical process is dominant. The obtained *b* values of the anodic and cathodic peaks are 0.81 and 0.82, respectively, indicating that the surface-controlled process dominates Li^+ storage in f-G-Si —which is mainly limited by the electrochemical reaction rate, but not the Li^+ ion diffusion process (Fig. 5d). These results shows that the Li^+ transport channels created *via* foaming endow f-G-Si with an efficient Li^+ diffusion pathway.

Conclusion

In summary, we have developed a facile and scalable preparation approach to establish efficient Li^+ transport channels in micro-sized Si/graphene composite anodes without sacrificing the capacity of Si. In our methodology, micro-sized Si particles

are encapsulated *via* conductive delaminated interconnected graphene layers, which act as the mechanically strong and flexible framework to buffer the volume changes during cycling. The highly conductive graphene layers and the established Li^+ transport channels endow micro-sized Si particles with superb electronic and ionic conductivity to achieve superior rate performance compared to the control samples. Due to its unique structural features, the prepared material, f-G-Si, can maximize the utilization of micro-sized Si and deliver outstanding electrochemical performance as a binder-free and free-standing anode without any additives. Our strategy targets the impending requirement of Si anodes to attain large capacity, excellent cycling stability, and superior high-rate performance at low cost. This concept can also be expanded to other materials that exhibit excellent stability and efficient electronic and ionic transport beyond silicon. The low-cost raw materials and scalable production process make low-cost and energy-dense anodes a realistic possibility.

Experiment

Materials

Graphene oxide solution in water (6 mg ml^{-1}) was purchased from GaoxiTech (Hangzhou Gaoxi Technology Co., Ltd). Silicon powder (1–5 microns, 99.9%) and $NH_2NH_2{\cdot}H_2O$ (99.9%) were purchased from Alfa Aesar. All supplied chemicals were used without further modification.

Synthesis of GO-Si

A suspension of 10 ml (6 mg ml^{-1}) of GO was sonicated for 10 minutes to obtain a homogenized suspension. Subsequently, 90 mg of micro-sized silicon was slowly added to the suspension (the weight ratio of Si to GO was 1 : 1.5) and stirred at 25 °C for 2 hours, forming an aqueous slurry. After that, the slurry was coated on a PET substrate by the blade coating method and dried at room temperature for 12 h. After drying, a dark brown film, GO-Si, was peeled off from the PET substrate.

Synthesis of f-G-Si and G-Si

The GO-Si film was immersed in a solution of hydrazine and water (N_2H_4/H_2O = 30 wt%) at room temperature (25 °C) for 10 minutes.[35] After drying at room temperature, the foamed graphene oxide/Si, f-GO-Si, was obtained. Finally, f-GO-Si was annealed at 850 °C under an argon atmosphere for 2 h, affording the foamed graphene/Si membrane (f-G-Si) with a thickness of 50 μm.

The GO-Si film was directly annealed at 850 °C under an argon atmosphere for 2 h, affording the graphene/Si membrane (G-Si) with a thickness of 10 μm.

Characterization

Field emission scanning electron microscopy (FESEM) was performed using a Hitachi SU-8220 model, operating at an accelerating voltage of 5.0 kV. High-resolution transmission electron microscopy (HRTEM) images were obtained using a Tecnai F20 model microscope. Powder X-ray diffraction (PXRD) data were recorded on a Rigaku model RINT Ultima III diffractometer between 10° and 80° with Cu Kα radiation (λ = 0.15418 nm). Thermogravimetric analysis (TGA) tests were performed on a Shimadzu DT-30B at a heating rate of 5 °C min^{-1} from room temperature to 1000 °C in the air environment. X-ray photoelectron spectroscopy (XPS) was conducted on ESCALAB250 apparatus at a base pressure of 1×10^{-9} mbar and an X-ray source of Cu Kα. The sheet resistance was measured using a four-probe tester (RTS-9).

Electrochemical measurement

The electrochemical performances of the f-G-Si, G-Si, and silicon anodes were evaluated using two-electrode CR2032 coin-type half-cells with lithium metal foil as a counter electrode, Celgard 2400 as a separator, and a solution of 1.2 M $LiPF_6$ in ethylene carbonate, diethyl carbonate and dimethyl carbonate (1 : 1 : 1, v/v) as an electrolyte. The f-G-Si and G-Si membranes were punched into circular disks with a diameter of 10 mm and directly used as the working electrode without further treatment. Both the mass loadings of f-G-Si and G-Si anodes were around 0.8–1 mg. For the control sample, the conventional Si anode using copper foil as the current collector was fabricated *via* a typical slurry method with micro-sized silicon, a conductive additive (Super P, Alfa Aesar), and the polyacrylic acid (PAA, a weight-average molecular weight of 240 000, Alfa Aesar) binder at a mass ratio of 7 : 2 : 1. All the coin-type cells were assembled in an Ar-filled glovebox (<0.1 ppm of oxygen and water). The cycling and rate capability tests were performed using a CT2001A battery program control test system within the voltage range of 0.01 to 2.0 V at 25 °C. The reported capacity was calculated based on the weight of active materials in the working electrode, and the coulombic efficiency was obtained as the ratio of the delithiation capacity to the lithiation capacity. EIS tests were carried out with frequency ranges of 0.01 Hz to 100 kHz on a BioLogic electrochemical workstation. The reaction kinetics was monitored by the GITT with a pulse current of 100 mA g^{-1} for 20 min between 20 min rest intervals. The apparent diffusion coefficient of Li^+ was studied based on Fick's second law following the simplified equation:

$$D = \frac{4}{\pi\tau}\left(\frac{m_B V_M}{M_B S}\right)^2\left(\frac{\Delta E_S}{\Delta E_\tau}\right)^2$$

where m_B and M_B are the active mass and molecular mass, respectively, V_M is the molar volume, S is the surface area of the electrode, and τ, ΔE_S, and ΔE_τ are the pulse time for charge and discharge processes, the voltage change in the steady state, and the voltage change during the pulse period, respectively.

The b value was calculated according to the following equation:

$$i = av^b$$

where i and v symbolize the peak current and scan rate, while a and b are variables, the b value could be obtained from the slope by plotting $\log(v)$ *vs.* $\log(i)$. Notably, a "b" value of 0.5 designates a diffusion-controlled process, while a "b" value of 1 designates a surface-controlled capacitive process.

Author contributions

X. L. and Y. M. conceived and designed the experiments. M. H. and S. Z. carried out materials synthesis and electrical measurements. W. X. and D. W. participated in part of the electrical measurements. X. L., Y. M., and M. H. co-wrote the paper. All authors discussed the results and commented on the manuscript.

Conflicts of interest

There are no conflicts to declare.

Acknowledgements

We gratefully acknowledge funding support from the National Natural Science Foundation of China (grant number 52173250) and the Zhejiang Provincial Market Supervision and Administration Bureau (grant number CY2023321). Mathar Hamza acknowledges the ANSO organization for a Ph.D. fellowship for this work.

References

1 M. Li, J. Lu, Z. Chen and K. Amine, *Adv. Mater.*, 2018, **30**, 1800561.
2 S. Lou, Z. Yu, Q. Liu, H. Wang, M. Chen and J. Wang, *Chem*, 2020, **6**, 2199–2218.
3 S. Lou, N. Sun, F. Zhang, Q. Liu and J. Wang, *Acc. Mater. Res.*, 2021, **2**, 1177–1189.
4 G. Yu, X. Xie, L. Pan, Z. Bao and Y. Cui, *Nano Energy*, 2013, **2**, 213–234.
5 B. Dunn, H. Kamath and J.-M. Tarascon, *Science*, 2011, **334**, 928–935.
6 D. Wang, W. Zhang, W. Zheng, X. Cui, T. Rojo and Q. Zhang, *Adv. Sci.*, 2017, **4**, 1600168.
7 J. Han, D.-M. Tang, D. Kong, F. Chen, J. Xiao, Z. Zhao, S. Pan, S. Wu and Q.-H. Yang, *Sci. Bull.*, 2020, **65**, 1563–1569.
8 I. Kovalenko, B. Zdyrko, A. Magasinski, B. Hertzberg, Z. Milicev, R. Burtovyy, I. Luzinov and G. Yushin, *Science*, 2011, **334**, 75–79.
9 J. Li, R. Lewis and J. Dahn, *Electrochem. Solid-State Lett.*, 2006, **10**, A17.
10 M. Zhou, X. Li, B. Wang, Y. Zhang, J. Ning, Z. Xiao, X. Zhang, Y. Chang and L. Zhi, *Nano Lett.*, 2015, **15**, 6222–6228.
11 M. L. Terranova, S. Orlanducci, E. Tamburri, V. Guglielmotti and M. Rossi, *J. Power Sources*, 2014, **246**, 167–177.
12 W. Luo, Y. Wang, S. Chou, Y. Xu, W. Li, B. Kong, S. X. Dou, H. K. Liu and J. Yang, *Nano Energy*, 2016, **27**, 255–264.
13 J. Hassoun, G. Derrien, S. Panero and B. Scrosati, *Adv. Mater.*, 2008, **20**, 3169–3175.
14 B. Wang, T. Qiu, X. Li, B. Luo, L. Hao, Y. Zhang and L. Zhi, *J. Mater. Chem. A*, 2015, **3**, 494–498.
15 S. Pan, J. Han, Y. Wang, Z. Li, F. Chen, Y. Guo, Z. Han, K. Xiao, Z. Yu, M. Yu, S. Wu, D.-W. Wang and Q.-H. Yang, *Adv. Mater.*, 2022, **34**, 2203617.
16 F. Chen, J. Han, D. Kong, Y. Yuan, J. Xiao, S. Wu, D.-M. Tang, Y. Deng, W. Lv, J. Lu, F. Kang and Q.-H. Yang, *Natl. Sci. Rev.*, 2021, **8**, nwab012.
17 X. Zhang, D. Wang, X. Qiu, Y. Ma, D. Kong, K. Müllen, X. Li and L. Zhi, *Nat. Commun.*, 2020, **11**, 3826.
18 L. Cao, T. Huang, M. Cui, J. Xu and R. Xiao, *Small*, 2021, **17**, 2005997.
19 A. Jamaluddin, B. Umesh, F. Chen, J.-K. Chang and C.-Y. Su, *Nanoscale*, 2020, **12**, 9616–9627.
20 W. Xu, C. Tang, N. Huang, A. Du, M. Wu, J. Zhang and H. Zhang, *Small Sci.*, 2022, **2**, 2100105.
21 D. Chen, R. Yi, S. Chen, T. Xu, M. L. Gordin and D. Wang, *Solid State Ionics*, 2014, **254**, 65–71.
22 J.-Z. Wang, C. Zhong, S.-L. Chou and H.-K. Liu, *Electrochem. Commun.*, 2010, **12**, 1467–1470.
23 A. R. Park, D.-Y. Son, J. S. Kim, J. Y. Lee, N.-G. Park, J. Park, J. K. Lee and P. J. Yoo, *ACS Appl. Mater. Interfaces*, 2015, **7**, 18483–18490.
24 W.-J. Meng, X.-Y. Han, Y.-L. Hou, Y. Xie, J. Zhang, C.-J. He and D.-L. Zhao, *Electrochim. Acta*, 2021, **382**, 138271.
25 H. Cai, K. Han, H. Jiang, J. Wang and H. Liu, *J. Phys. Chem. Solids*, 2017, **109**, 9–17.
26 K. Fu, O. Yildiz, H. Bhanushali, Y. Wang, K. Stano, L. Xue, X. Zhang and P. D. Bradford, *Adv. Mater.*, 2013, **25**, 5109–5114.
27 J. Yang, Y. Wang, W. Li, L. Wang, Y. Fan, W. Jiang, W. Luo, Y. Wang, B. Kong and C. Selomulya, *Adv. Mater.*, 2017, **29**, 1700523.
28 C. Yu, X. Lin, X. Chen, L. Qin, Z. Xiao, C. Zhang, R. Zhang and F. Wei, *Nano Lett.*, 2020, **20**, 5176–5184.
29 J. Lin, J. He, Y. Chen, Q. Li, B. Yu, C. Xu and W. Zhang, *Electrochim. Acta*, 2016, **215**, 667–673.
30 S. Chae, M. Ko, S. Park, N. Kim, J. Ma and J. Cho, *Energy Environ. Sci.*, 2016, **9**, 1251–1257.
31 R. Jain, A. S. Lakhnot, K. Bhimani, S. Sharma, V. Mahajani, R. A. Panchal, M. Kamble, F. Han, C. Wang and N. Koratkar, *Nat. Rev. Mater.*, 2022, **7**, 736–746.
32 Z. Y. Zhang, Z. W. Li, Q. Luo, B. Z. Yang, Y. Liu, Y. Y. Hu, X. B. Liu, Y. H. Yin, Y. S. Li and Z. P. Wu, *Carbon*, 2022, **188**, 238–245.
33 X. Zhang, H. Wang, R. I. Pushparaj, M. Mann and X. Hou, *Electrochim. Acta*, 2022, **434**, 141329.

34 M. S. Kang, I. Heo, S. Kim, J. Yang, J. Kim, S.-J. Min, J. Chae and W. C. Yoo, *Energy Storage Mater.*, 2022, **50**, 234–242.
35 K. Pang, X. Song, Z. Xu, X. Liu, Y. Liu, L. Zhong, Y. Peng, J. Wang, J. Zhou and F. Meng, *Sci. Adv.*, 2020, **6**, eabd4045.
36 V. Chabot, K. Feng, H. W. Park, F. M. Hassan, A. R. Elsayed, A. Yu, X. Xiao and Z. Chen, *Electrochim. Acta*, 2014, **130**, 127–134.
37 H. Zhang, S. Jing, Y. Hu, H. Jiang and C. Li, *J. Power Sources*, 2016, **307**, 214–219.
38 H. Jiang, X. Zhou, G. Liu, Y. Zhou, H. Ye, Y. Liu and K. Han, *Electrochim. Acta*, 2016, **188**, 777–784.
39 D. P. Wong, H.-P. Tseng, Y.-T. Chen, B.-J. Hwang, L.-C. Chen and K.-H. Chen, *Carbon*, 2013, **63**, 397–403.
40 Q. Xu, J. Y. Li, J. K. Sun, Y. X. Yin, L. J. Wan and Y. G. Guo, *Adv. Energy Mater.*, 2017, **7**, 1601481.
41 B. Lee, T. Liu, S. K. Kim, H. Chang, K. Eom, L. Xie, S. Chen, H. D. Jang and S. W. Lee, *Carbon*, 2017, **119**, 438–445.
42 F. Lyu, Z. Sun, B. Nan, S. Yu, L. Cao, M. Yang, M. Li, W. Wang, S. Wu and S. Zeng, *ACS Appl. Mater. Interfaces*, 2017, **9**, 10699–10707.
43 S. Huang, L.-Z. Cheong, D. Wang and C. Shen, *ACS Appl. Mater. Interfaces*, 2017, **9**, 23672–23678.
44 C. Wang, H. Wu, Z. Chen, M. T. McDowell, Y. Cui and Z. Bao, *Nat. Chem.*, 2013, **5**, 1042–1048.
45 Y. Li, K. Yan, H.-W. Lee, Z. Lu, N. Liu and Y. Cui, *Nat. Energy*, 2016, **1**, 1–9.
46 S. Choi, T.-W. Kwon, A. Coskun and J. W. Choi, *Science*, 2017, **357**, 279–283.
47 D. Wang, M. Gao, H. Pan, Y. Liu, J. Wang, S. Li and H. Ge, *J. Alloys Compd.*, 2014, **604**, 130–136.
48 X. Zhang, R. Guo, X. Li and L. Zhi, *Small*, 2018, **14**, 1800752.